


Effective gyration of polar vortex arrays controlled by high orbital angular momentum of light

Lingyuan Gao , Sergei Prokhorenko, Yousra Nahas, and Laurent Bellaïche*
*Physics Department and Institute for Nanoscience and Engineering, University of Arkansas,
 Fayetteville, Arkansas 72701, USA*



(Received 13 November 2023; revised 1 February 2024; accepted 21 February 2024; published 15 March 2024)

The electric field of an optical vortex (OV) beam displays a specific winding pattern determined by its spatial variation and angular momentum. An OV beam can serve as an optical spanner, which exerts a force torque to rotate particles around the beam axis. In this work, using first-principles-based calculations, we demonstrate that an OV beam with high orbital angular momentum (OAM) can induce local electric dipoles to self-order and form a vortex array distributed along azimuthal directions. More importantly, owing to its intrinsic symmetry, the evolution of the vortex array with time can be viewed as an effective spinning around the central axis, while its rotation speed is also connected to the OAM value. Our study thus presents an alternative approach for manipulating polar vortices using the optical field apart from mechanical and electric stimuli, and especially for a deterministic control of vortex dynamics that is critical in the application of memory devices.

DOI: [10.1103/PhysRevB.109.L121110](https://doi.org/10.1103/PhysRevB.109.L121110)

Light beams established on the Laguerre-Gaussian (LG) mode set was invented in the laboratory by Allen *et al.* more than three decades ago [1]. Such beams carry an orbital angular momentum (OAM) defined by the phase factor $e^{im\phi}$, where ϕ is the azimuthal angle and m is an integer associated with photon's OAM $m\hbar$. In addition to the helical wave front denoted by $e^{im\phi}$, LG beams are characterized by an annular profile of the light intensity $(\frac{r}{w})^{|m|} e^{-\frac{r^2}{w^2}}$. As a result, the intensity gradient along the radial direction generates a “gradient force” that drives small particles to move towards the beam focus, while the phase gradient along the azimuthal angle direction generates a “scattering force” that can circulate particles on the annular ring of LG beams via light absorption [2–5]. Therefore, LG beams are also known as “optical tweezers” or “optical spanners,” as they can manipulate the motion of particles ranging from nanometers to micrometers [6,7].

For a circularly polarized LG light beam, its two-dimensional (2D) electric or magnetic field is naturally endowed with a winding number, $-m \cdot \sigma$, where σ denotes the helicity of the light [8]. The winding number, as an integer, quantifies the number of times the vector field completes a rotation of 2π as it encircles the center of the beam, where the intensity of the field is zero and the direction of the field cannot be defined [9]. This singularity, together with the entire whirling configuration, presents the field as an $SO(2)$ “optical vortex” (OV), which cannot be smoothly deformed into a linearly polarized light and is commonly recognized as a topological defect in 2D space [10,11]. The vortexlike structures manifest in various exotic phases and condensed-matter systems, including superfluids, superconductors, and magnetic media [12–15]. Rapid progress has also been made in exploring ferroelectric vortices built by electric dipoles. They were theoretically predicted in ferroelectric nanodisks and nanodots in the early 2000s [16,17] and were not

revealed in experiments until 2016: Yadav *et al.* showed ordered arrays of vortex pairs formed in $\text{PbTiO}_3/\text{SrTiO}_3$ [18], which later exhibited fascinating phenomena such as emergent chirality and negative capacitance [19,20]. Different from the Dzyaloshinsky-Moriya interaction rising from the interplay between spin-orbit coupling and superexchange in magnetic systems [21,22], the complex dipolar textures in ferroelectrics emerge from the competition among electrostatic, elastic, and gradient energies [23,24].

One critical step of utilizing polar vortices in applications is to robustly handle vortices with external control. Experiments have shown that by applying the electric field, conversion between vortex and stripe phases [25], and a reversal of chirality in polar vortices [26], can be achieved. Beyond the static electric field, subpicosecond light pulses with above-band-gap-excitation can convert the vortex array into supercrystals [27]; the THz field can drive collective sub-THz dynamics of polar vortices, such as a transverse oscillation at 0.08 THz [28,29]. However, to the best of our knowledge, how to move polar vortices in a controllable manner still remains unknown.

In this work, using atomistic simulations based on first-principles calculations, we validate the idea of converting optical vortices to dynamical polar vortices, by making the unique optical field–LG beams at THz frequency interact with ferroelectric materials. Intriguingly, the beam not only induces the formation of polar vortices but also manipulates their motion in a controllable way. For a specific OAM value m , the winding pattern of the electric field exhibits a symmetrical profile, and its coupling with electric dipoles gives rise to the formation of a polar vortex array in ferroelectric ultrathin films. Vortices with opposite chirality are positioned next to each other on an annular ring, and their configurations evolve with the time-dependent field. This can be equivalently viewed as a spinning of the whole vortex array around the beam center at the same frequency of the THz optical field, which we call “effective gyration.”

*Corresponding author: laurent@uark.edu

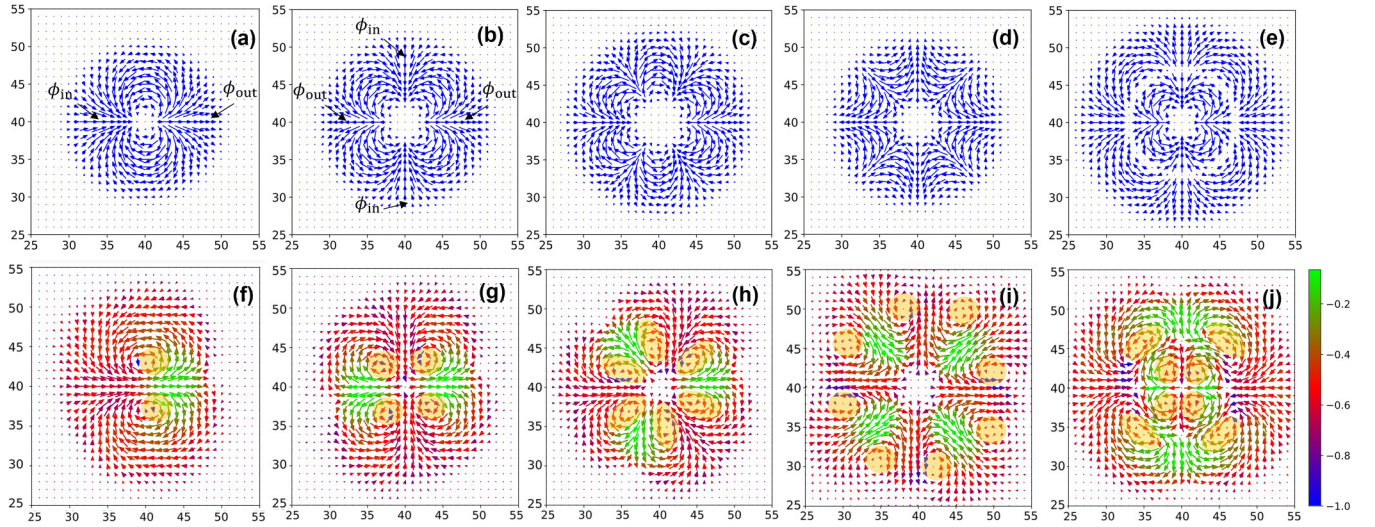


FIG. 1. Display of electric field patterns of various LG beams (first row) and of corresponding polar vortex arrays (second row) at $t = pT$. The x and y axes correspond to site numbers along two in-plane directions of the film. (a)–(d) $l = 0$ and $m = -2, -3, -4$, and 3 . (e) $l = 1$ and $m = -3$. ϕ_{in} and ϕ_{out} denoting the respective azimuthal angles of ingoing and outgoing fields are highlighted by arrows in panels (a) and (b). In panel (d), the electric field displays as an antivortex at the center of the plane. (f)–(j) Polar vortex arrays formed under corresponding LG beams in the first row [in the order of panels (a)–(e)]. The out-of-plane P_z component is normalized and denoted with the colorbar. The core of each vortex is highlighted by the yellow shaded area.

Electric field of the LG beam. The electric field of the LG beam can be generally described as

$$\vec{E}(r, \phi, z = 0) = E_0 C_{lm} \frac{1}{w} \left(\frac{\sqrt{2}r}{w} \right)^{|m|} e^{-\frac{r^2}{w^2}} L_l^{|m|} \left(\frac{2r^2}{w^2} \right) [\cos(m\phi - \omega t) \vec{e}_x - \sigma \sin(m\phi - \omega t) \vec{e}_y]. \quad (1)$$

In the equation above, E_0 and w denote the magnitude and the beam radius of the electric field, respectively. C_{lm} is the normalization constant, $L_l^{|m|}$ is the generalized Laguerre polynomial, and l is the node index. Here we adopt $\sigma = +1$ to fix the helicity as left-polarized.

We first examine fields with $l = 0$. In this instance, $C_{lm} = 1$ is a constant. Figures 1(a)–1(c) illustrate the field configuration when $m = -2, -3$, and -4 at $t = pT$ (where p is a positive integer and T denotes the period of the field). To have a better contrast between the field [Figs. 1(a)–1(e)] and the response of on-site dipoles [Figs. 1(f)–1(j)], we plot both fields and dipoles in the dimension of the simulation supercell (introduced below). There is only one radial node (namely, the local maximum intensity is on a ring with a radius of $\sim \sqrt{2}w$), and the field magnitude decreases radially from the ring in both the inward and outward directions. At the center (the origin of the cylindrical coordinates), E decreases to zero. At $t = pT$, according to Eq. (1), the orientation of the field at (r, ϕ) is fully determined by its azimuthal angle ϕ , and the extent of $\vec{E}(r, \phi)$'s rotation increases with the OAM magnitude $|m|$. In particular, for fields radially oriented towards or away from the center of the beam, their azimuthal angles are given by

$$\begin{aligned} -m\phi_{\text{in}} &= \phi_{\text{in}} + (2n - 1)\pi, \\ -m\phi_{\text{out}} &= \phi_{\text{out}} + (2n)\pi. \end{aligned} \quad (2)$$

In the equation above, n is an integer, and we use subscripts “in” and “out” to denote the flowing direction of the field. As shown in the plot, lines oriented along $\phi_{\text{in}} = \frac{(2n-1)\pi}{(-m-1)}$ and $\phi_{\text{out}} = \frac{2n\pi}{(-m-1)}$ separate the whole plane into several subregions: in each subregion, the out-going fields flow away from the center along one boundary (ϕ_{out}), adjust their orientations along the contour, and flow towards the center along the other boundary (ϕ_{in}) to form a flux-closure domain. Symmetrywise, in a 2D field, these lines serve as symmetry axes, relative to which reflection operations can be performed between these domains. In addition to reflection, twofold and threefold rotations can also map one domain to another in Figs. 1(b) and 1(c), indicating field patterns there belonging to two-dimensional D_2 and D_3 groups, respectively. Note in Eq. (2), no solution exists for $m = -1$; this is due to the fact that the change of the field orientation for $m = -1$ cannot exceed 2π even making a full contour. Thus, symmetric subregions fail to develop, leading the field to exhibit varied shapes at different t values [30].

We next examine cases when the field pattern is more complicated.

(i) For $m > 0$, symmetric subregions form for all m (including $m = 1$) with a symmetry of $C_{m+1,v}$, while each subregion is an open-flux domain: the field flows in along one boundary (ϕ_{in}), but exhibits an anticrossing behavior at the center, and flows out along the other boundary (ϕ_{out}). Similar to $m < 0$, $\phi_{\text{in}} = \frac{(2n-1)\pi}{(m+1)}$ and $\phi_{\text{out}} = \frac{2n\pi}{(m+1)}$ can be easily derived for $m > 0$.

(ii) For $l > 0$, along the radial direction, there are $l + 1$ nodes with the local maximal intensity and l nodes with zero field intensity, resulting in the formation of l bright annular rings. We illustrate these two cases with $l = 0$ and $m = 3$ and with $l = 1$ and $m = -3$ in Figs. 1(d) and 1(e), respectively.

The intriguing field patterns of LG beams enlighten us to consider writing such symmetric optical textures in real materials. An active response from the material to local optical field at a microscopic level is required to achieve such a goal. Order parameters, such as electric dipoles or magnetic moments, reside continuously on lattices over a long range and respond to optical fields promptly, naturally fulfilling this criterion. Former studies have investigated the response of magnetic materials to magnetic fields of LG beams [31–33]; here, we do not focus on magnetic compounds but rather on nonmagnetic, ferroelectric materials, where the response to the electric field part is more crucial.

Polar vortex array induced by the LG beam. Experimentally observed polar vortex is at a scale of tens of unit cells [18]. Therefore, we choose the prototype ferroelectric ultrathin films $\text{Pb}(\text{Zr}_{0.4}\text{Ti}_{0.6})\text{O}_3$ (PZT) in the $80 \times 80 \times 5$ supercell grown along the [001] direction as the modeling system, where each unit cell has a lattice constant of 0.4 nm. The unit of a polar vortex is an on-site electric dipole \mathbf{p}_i in cell i , essentially representing an off-centering ion displacement \mathbf{u}_i . In the ferroelectric phase transition, such displacements rise from the condensation of soft modes. Therefore, we adopt the effective Hamiltonian computational approach, which defines a restricted Born-Oppenheimer potential energy surface with soft modes and acoustic modes fitted from first-principles calculations [34–36]. The method has demonstrated remarkable success in predicting diverse exotic polar structures characterized by atomic distortions in PZT systems [17,37–44]. We perform molecular dynamics simulations to explore the potential energy landscape and all possible dipolar configurations when the electric field of the LG beam is introduced in a continuous wave form to a well-equilibrated monodomain configuration at 10 K: with all dipoles aligning along $[00\bar{1}]$ —the out-of-plane z direction, we let the light propagate along the z axis, so that the electric field, which only has in-plane x and y components, interacts with the in-plane part of the dipoles. The polarization magnitude in the poled monodomain is computed to be $73 \mu\text{C}/\text{cm}^2$, close to experimental measurements [45–47]. Considering the dimension of the system and the response time of soft modes, we choose $w = 5$ unit cells (u.c.) and $\omega = 1$ THz as the beam radius and the light frequency, respectively. The maximal magnitude E_{max} for different values of l and m is set with respect to an experimental value at the order of 10^8 V/m [48,49]. Computational methods and details can be found in the Supplemental Material [50].

Figures 1(f)–1(h) display the respective polar textures at the bottom (001) layer captured at approximately $t = pT$ after dipoles establish a cyclic motion since fields shown in Figs. 1(a)–1(c) are introduced to the system. A time delay of approximately 0.1 ps is needed for dipoles to fully align with field vectors (see Fig. S4 and relevant discussions in the Supplemental Material [50]). In-plane components of polar textures resemble electric fields in that they share similar winding patterns and the same two-dimensional $D_{|m|+1}$ symmetry. Side-view plots shown in Fig. S1 in the Supplemental Material [50] reveal that the magnitude of P_x developed in the central region is comparable to that of P_z in the poled monodomain. Nevertheless, differences between dipoles and fields are notable: rather than strictly adhering to the

orientation of the on-site field and adopting a flux-closure pattern, dipoles arrange their orientations and form a vortex in each subregion. For example, in the case of $m = -2$ [Fig. 1(f)], dipoles at $x = 40$ and $y = 41$ and 42 point along the $+x$ direction and are antiparallel to dipoles at $x = 40$ and $y > 43$ (e.g., $\phi = \frac{\pi}{2}$), while all corresponding field vectors at this azimuthal angle point along the $-x$ direction [Fig. 1(a)]. In another case of $m = -3$ [Fig. 1(g)], in the yellow shaded area within each quadrant, four neighboring dipoles change their orientations continuously and overall rotate by 2π and exhibit as the center of the vortex located in each quadrant, while corresponding field vectors in Fig. 1(b) only differ by an angle less than $\frac{\pi}{2}$. Note with an increasing $|m|$, domains confined by ϕ_{in} and ϕ_{out} get narrower along the azimuthal direction, while the vortex in each domain extends along the radial direction, as illustrated in the case of $m = -4$ shown in Fig. 1(h). In all cases, dictated by orientations of field vectors on the boundary of each domain, neighboring vortices display opposite chiralities. Note that the generation of polar vortex array remains robust even with a 1 order of magnitude reduction in the field magnitude (see Fig. S3 in the Supplemental Material [50]).

Emergence of polar vortices can be explained as follows. At sites where the electric fields E_i are relatively large, the electrostatic energy $-\mathbf{E}_i \cdot \mathbf{p}_i$ is the dominant term; dipoles thus tend to align with the on-site electric field in order to minimize the electrostatic energy introduced by light and reduce the total energy. In contrast, in the region where E_i are small, other energy contributions, including polarization gradient and polarization anisotropy [51], compete with the electrostatic energy; such anisotropy energy can be lowered by a progressive rotation of the polarization [18]. Additionally, when $r \rightarrow 0$, the orientation of the field undergoes a significant alteration owing to the factor of $m\phi$, despite the field magnitude $E \rightarrow 0$. If in-plane components of \mathbf{p}_i align with E_i at $r \rightarrow 0$, a large bound charge ρ_b resulting from $\nabla \cdot \mathbf{P}$ will be created in the central region, which will substantially increase the electrostatic energy [52,53]. Taken together, this gives rise to the formation of vortices, where dipoles change their orientations continuously and form closed loops within each subregion. This is consistent with nanodomains in ferroelectric ultrathin films, where vortices emerge to preserve the charge neutralities at surfaces and to reduce the electrostatic energy associated with the depolarization field and the anisotropy energy [24,37,54,55]. For reference, without showing energy relevant to phenomenological models, different energy terms in effective Hamiltonians based on atomistic models, including on-site soft mode energies, short-range interaction energies, elastic energies, elastic-soft-mode coupling energies, dipole-dipole interaction energies, and electrostatic energies from coupling to the external field, have been plotted versus time in Fig. S2 in the Supplemental Material [50].

When considering positive m , a dipolar antivortex with notable in-plane components emerges in response to the anticrossing electric field, while $2(|m| + 1)$ vortices are distributed in each sector of the antivortex [see Fig. 1(i) for $l = 0$ and $m = 3$]. As vortices are located relatively distant from the center, the local electric fields are comparably smaller, resulting in constituent dipoles of vortices possessing

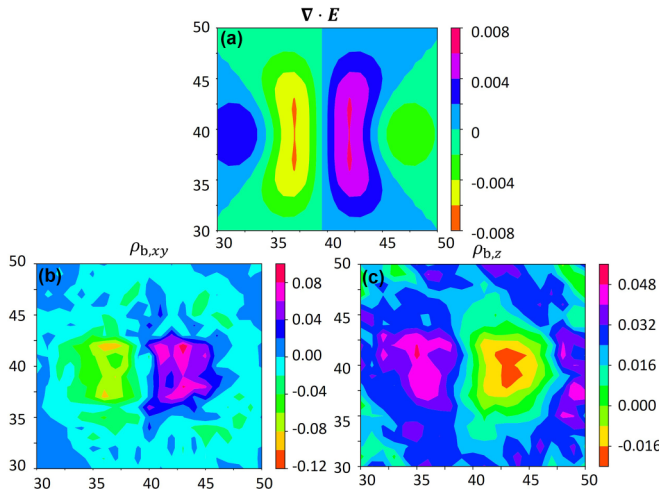


FIG. 2. The divergence of (a) the electric field of the LG beam with $l = 0$ and $m = -2$, (b) dipole components $P_{x,y}$ (which is the bound charge component $\rho_{b,xy}$), and (c) P_z ($\rho_{b,z}$).

minor in-plane components. Nevertheless, these modest in-plane components manage to organize in a closed loop, giving rise to the formation of vortices. Figure 1(j) illustrates the dipolar pattern for $l = 1$ and $m = -3$. For the nodal index $l = 1$, an additional ring of vortices emerges at a greater radius, encircling the inner vortex array of $l = 0$. The emerging ring of vortices consists of four elliptical vortices, aligning with the region where the field intensity approaches zero (also in a ringlike shape). Consistent with the preceding analysis, dipoles within this region can robustly adapt their orientations and manage to form a closed loop alongside the significant but antiparallel in-plane dipoles inside and outside the ringlike area. The self-organized and widely distributed vortex textures highlight the importance of the polarization gradient and the anisotropy energy among all competing energy contributions.

We next focus on the out-of-plane (z) components of vortices. While all z components are negative across the plane, their magnitudes vary by locations and depend on the on-site in-plane (x, y) components. Since only $P_{x,y}$ are directly coupled with light, P_z varies more as a response to $P_{x,y}$ to ensure a small bound charge ρ_b , which is the sum of $\rho_{b,xy}$ and $\rho_{b,z}$. These two latter charges are the divergence to $P_x + P_y$ and P_z , respectively. In a previous study, an LG beam with $l = 0$ and $m = -1$ induced the creation of “Neel”-type skyrmions at specific times, of which P_z values near the plane center switch their negative values to positive values [30]. The switching results from the convergent or divergent form of $E_{x,y}$ as well as $P_{x,y}$, and that causes a large bound charge $\rho_{b,xy}$ emerging at the center. To reduce the overall ρ_b , P_z varies drastically so that $\rho_{b,z}$ can compensate $\rho_{b,xy}$. For $m \neq -1$, the chiral patterns of $E_{x,y}$ and $P_{x,y}$ exhibit divergence-free behaviors and only a small $\rho_{b,xy}$ is created. Therefore, a small $\rho_{b,z}$ is induced and P_z can maintain their negative values and vary smoothly throughout the plane. Figures 2(a) and 2(b) present the divergence of the electric field $\frac{\partial E_x}{\partial x} + \frac{\partial E_y}{\partial y}$ and the divergence of in-plane dipole components $\frac{\partial P_x}{\partial x} + \frac{\partial P_y}{\partial y}$ (namely, $\rho_{b,xy}$) in the case of $l = 0$ and $m = -2$, respectively. As revealed in Figs. 1(a) and 1(f), $P_{x,y}$ follows a pattern close to that of $E_{x,y}$,

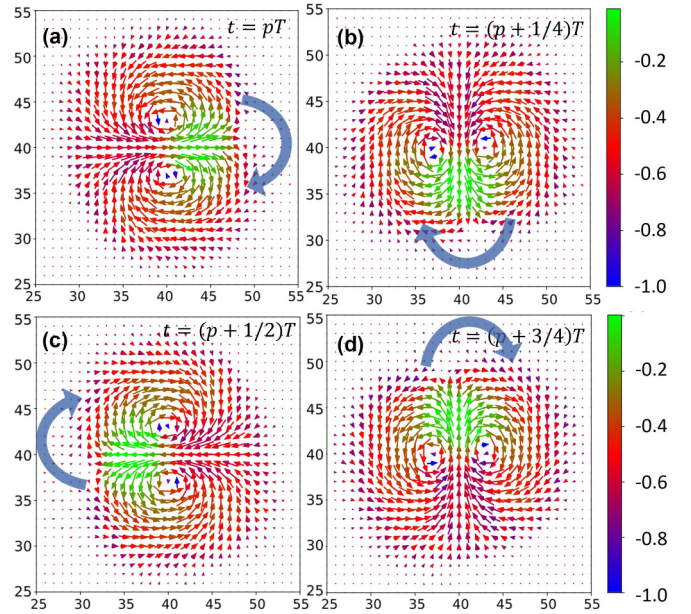


FIG. 3. The displayed dipole pattern for $l = 0$ and $m = -2$ at different times t , as written in each panel. Yellow arrows denote the rotation direction of polar vortex arrays.

so the divergence of $E_{x,y}$ and the divergence of $P_{x,y}$ share similarities, featuring two regions with opposite values along the x axis. This further induces a $\rho_{b,z}$ contrary to $\rho_{b,xy}$ in these regions [Fig. 2(c)], which finally determines that P_z at the (001) bottom layer adopt large negative values on the left side and small negative values on the right side of the x axis [see Fig. 1(f)]. In areas in between, P_z undergoes a gradual variation as a transition.

Effective gyration of polar vortex arrays. For a left-polarized LG beam, phases of electric field vectors increase by ωt as time progresses, leading to a counterclockwise rotation at each site. In addition, with a negative OAM value of $m \neq -1$, the orienting angle of the on-site electric field vector increases with the azimuthal angle ϕ as $-m\phi$. Consequently, electric field vectors situated at larger ϕ at earlier times will align similarly to vectors situated at smaller ϕ at later times, resulting in an overall appearance of a “clockwise rotation” of the entire field pattern. Former have studies already demonstrated that a LG beam can trap or displace a single particle by gradient or scattering force [2–4]; now we wonder whether this dynamical feature of optical fields can be utilized to “spin” dipolar textures by driving a collective motion. Dipoles reside continuously over the lattice so every dipole interacts with the on-site field across the entire plane. Also, dipoles can reorient their directions readily to the dynamical field at THz frequency at all times. Thus, the “progressive rotation” belonging to the dynamical optical field can be reproduced in a vortex array.

Figures 3(a)–3(d) present the in-plane view about the polar vortex array corresponding to $l = 0$ and $m = -2$ at four different times starting from $t = pT$ to $(p + \frac{3}{4})T$ with an interval of $\frac{1}{4}T$. We use notations ϕ_{in} and ϕ_{out} , similar to those we use for the electric field in Fig. 1, to denote azimuthal angles where in-plane dipole components point radially inward or outward, respectively. The sequence of

snapshots witnesses a complete gyration of the vortex array by an angle of 2π within a single period T , marked by the variation $\Delta\phi_{\text{in/out}} = \frac{\pi}{2}$ within an interval of $\frac{T}{4}$. Taking the distance from the vortex core to the center of the plane r_v as 3 u.c., the traveling speed of vortex array v can be approximated as $v = 2\pi r_v/T \approx 6000$ m/s, much faster than that of a magnetic skyrmion [32,33].

It is evident that by adjusting the frequency ω and the chirality σ of the light, the gyration speed and its direction can also be modulated. Furthermore, we want to point out that there is an intrinsic connection between the gyration speed and the OAM value m . A “complete” gyration refers to $\phi_{\text{in/out}}$ as the boundary of one subregion moving to $\phi_{\text{in/out}}$ of the next subregion. Thus, based on Eq. (1), depending on m , a general expression of the gyration velocity can be given by

$$v = \frac{2\pi r_v}{(-m-1)T} (m < 0), \quad v = -\frac{2\pi r_v}{(m+1)T} (m > 0). \quad (3)$$

This indicates that an LG beam with a lower value of m can actually spin the vortex array more efficiently.

In summary, we demonstrate the idea of converting optical vortices to polar vortices in ferroelectric ultrathin films. Furthermore, the time evolution of a THz dynamical field induces a “gyration effect” of polar vortex arrays, causing them to rotate around the central axis at a speed synchronizing with the optical field. Our study presents an alternative scenario for creating electric vortices and manipulating their motions with optical signals.

Acknowledgments. We acknowledge support from the Grant MURI ETHOS W911NF-21-2-0162 from the Army Research Office (ARO), ARO Grant No. W911NF-21-1-0113, and the Vannevar Bush Faculty Fellowship (VBFF) Grant No. N00014-20-1-2834 from the Department of Defense. We also acknowledge the computational support from the Arkansas High Performance Computing Center and the HPCMP Pathfinder Award for computational resources.

-
- [1] L. Allen, M. W. Beijersbergen, R. J. C. Spreeuw, and J. P. Woerdman, Orbital angular momentum of light and the transformation of Laguerre-Gaussian laser modes, *Phys. Rev. A* **45**, 8185 (1992).
- [2] H. He, M. E. J. Friese, N. R. Heckenberg, and H. Rubinsztein-Dunlop, Direct observation of transfer of angular momentum to absorptive particles from a laser beam with a phase singularity, *Phys. Rev. Lett.* **75**, 826 (1995).
- [3] M. E. J. Friese, J. Enger, H. Rubinsztein-Dunlop, and N. R. Heckenberg, Optical angular-momentum transfer to trapped absorbing particles, *Phys. Rev. A* **54**, 1593 (1996).
- [4] M. Dienerowitz, M. Mazilu, P. J. Reece, T. F. Krauss, and K. Dholakia, Optical vortex trap for resonant confinement of metal nanoparticles, *Opt. Express* **16**, 4991 (2008).
- [5] M. Padgett and R. Bowman, Tweezers with a twist, *Nat. Photon.* **5**, 343 (2011).
- [6] N. Simpson, L. Allen, and M. Padgett, Optical tweezers and optical spanners with Laguerre–Gaussian modes, *J. Mod. Opt.* **43**, 2485 (1996).
- [7] D. G. Grier, A revolution in optical manipulation, *Nature (London)* **424**, 810 (2003).
- [8] K. Shintani, K. Taguchi, Y. Tanaka, and Y. Kawaguchi, Spin and charge transport induced by a twisted light beam on the surface of a topological insulator, *Phys. Rev. B* **93**, 195415 (2016).
- [9] A. Beekman, L. Rademaker, and J. van Wezel, An introduction to spontaneous symmetry breaking, *SciPost Phys. Lect. Notes*, **11** (2019).
- [10] J. M. Kosterlitz and D. J. Thouless, Ordering, metastability and phase transitions in two-dimensional systems, *J. Phys. C* **6**, 1181 (1973).
- [11] N. D. Mermin, The topological theory of defects in ordered media, *Rev. Mod. Phys.* **51**, 591 (1979).
- [12] D. J. Bishop and J. D. Reppy, Study of the superfluid transition in two-dimensional ^4He films, *Phys. Rev. Lett.* **40**, 1727 (1978).
- [13] G. Blatter, M. V. Feigel'man, V. B. Geshkenbein, A. I. Larkin, and V. M. Vinokur, Vortices in high-temperature superconductors, *Rev. Mod. Phys.* **66**, 1125 (1994).
- [14] T. Shinjo, T. Okuno, R. Hassdorf, K. Shigeto, and T. Ono, Magnetic vortex core observation in circular dots of permalloy, *Science* **289**, 930 (2000).
- [15] A. Wachowiak, J. Wiebe, M. Bode, O. Pietzsch, M. Morgenstern, and R. Wiesendanger, Direct observation of internal spin structure of magnetic vortex cores, *Science* **298**, 577 (2002).
- [16] H. Fu and L. Bellaïche, Ferroelectricity in barium titanate quantum dots and wires, *Phys. Rev. Lett.* **91**, 257601 (2003).
- [17] I. I. Naumov, L. Bellaïche, and H. Fu, Unusual phase transitions in ferroelectric nanodisks and nanorods, *Nature (London)* **432**, 737 (2004).
- [18] A. Yadav, C. Nelson, S. Hsu, Z. Hong, J. Clarkson, C. Schlepütz, A. Damodaran, P. Shafer, E. Arenholz, L. Dedon *et al.*, Observation of polar vortices in oxide superlattices, *Nature (London)* **530**, 198 (2016).
- [19] P. Shafer, P. García-Fernández, P. Aguado-Puente, A. R. Damodaran, A. K. Yadav, C. T. Nelson, S.-L. Hsu, J. C. Wojdeł, J. Íñiguez, L. W. Martin *et al.*, Emergent chirality in the electric polarization texture of titanate superlattices, *Proc. Natl. Acad. Sci. USA* **115**, 915 (2018).
- [20] A. K. Yadav, K. X. Nguyen, Z. Hong, P. García-Fernández, P. Aguado-Puente, C. T. Nelson, S. Das, B. Prasad, D. Kwon, S. Cheema *et al.*, Spatially resolved steady-state negative capacitance, *Nature (London)* **565**, 468 (2019).
- [21] I. Dzyaloshinsky, A thermodynamic theory of “weak” ferromagnetism of antiferromagnetics, *J. Phys. Chem. Solids* **4**, 241 (1958).
- [22] T. Moriya, Anisotropic superexchange interaction and weak ferromagnetism, *Phys. Rev.* **120**, 91 (1960).
- [23] S. Chen, S. Yuan, Z. Hou, Y. Tang, J. Zhang, T. Wang, K. Li, W. Zhao, X. Liu, L. Chen *et al.*, Recent progress on topological structures in ferroic thin films and heterostructures, *Adv. Mater.* **33**, 2000857 (2021).
- [24] J. Junquera, Y. Nahas, S. Prokhorenko, L. Bellaïche, J. Íñiguez, D. G. Schlom, L.-Q. Chen, S. Salahuddin, D. A. Muller, L. W. Martin, and R. Ramesh, Topological phases in polar oxide nanostructures, *Rev. Mod. Phys.* **95**, 025001 (2023).

- [25] A. R. Damodaran, J. Clarkson, Z. Hong, H. Liu, A. K. Yadav, C. T. Nelson, S.-L. Hsu, M. McCarter, K.-D. Park, V. Kravtsov *et al.*, Phase coexistence and electric-field control of toroidal order in oxide superlattices, *Nat. Mater.* **16**, 1003 (2017).
- [26] P. Behera, M. A. May, F. Gómez-Ortiz, S. Susarla, S. Das, C. T. Nelson, L. Caretta, S.-L. Hsu, M. R. McCarter, B. H. Savitzky *et al.*, Electric field control of chirality, *Sci. Adv.* **8**, eabj8030 (2022).
- [27] V. Stoica, N. Laanait, C. Dai, Z. Hong, Y. Yuan, Z. Zhang, S. Lei, M. McCarter, A. Yadav, A. Damodaran *et al.*, Optical creation of a supercrystal with three-dimensional nanoscale periodicity, *Nat. Mater.* **18**, 377 (2019).
- [28] Q. Li, V. A. Stoica, M. Paściak, Y. Zhu, Y. Yuan, T. Yang, M. R. McCarter, S. Das, A. K. Yadav, S. Park *et al.*, Subterahertz collective dynamics of polar vortices, *Nature (London)* **592**, 376 (2021).
- [29] T. Yang, C. Dai, Q. Li, H. Wen, and L.-Q. Chen, Condensation of collective polar vortex modes, *Phys. Rev. B* **103**, L220303 (2021).
- [30] L. Gao, S. Prokhorenko, Y. Nahas, and L. Bellaiche, Dynamical control of topology in polar skyrmions via twisted light, *Phys. Rev. Lett.* **132**, 026902 (2024).
- [31] H. Fujita and M. Sato, Encoding orbital angular momentum of light in magnets, *Phys. Rev. B* **96**, 060407(R) (2017).
- [32] W. Yang, H. Yang, Y. Cao, and P. Yan, Photonic orbital angular momentum transfer and magnetic skyrmion rotation, *Opt. Express* **26**, 8778 (2018).
- [33] S. H. Guan, Y. Liu, Z. P. Hou, D. Y. Chen, Z. Fan, M. Zeng, X. B. Lu, X. S. Gao, M. H. Qin, and J.-M. Liu, Optically controlled ultrafast dynamics of skyrmion in antiferromagnets, *Phys. Rev. B* **107**, 214429 (2023).
- [34] W. Zhong, D. Vanderbilt, and K. M. Rabe, Phase transitions in BaTiO₃ from first principles, *Phys. Rev. Lett.* **73**, 1861 (1994).
- [35] W. Zhong, D. Vanderbilt, and K. Rabe, First-principles theory of ferroelectric phase transitions for perovskites: The case of BaTiO₃, *Phys. Rev. B* **52**, 6301 (1995).
- [36] P. Ghosez and J. Junquera, Modeling of ferroelectric oxide perovskites: From first to second principles, *Annu. Rev. Condens. Matter Phys.* **13**, 325 (2022).
- [37] I. Kornev, H. Fu, and L. Bellaiche, Ultrathin films of ferroelectric solid solutions under a residual depolarizing field, *Phys. Rev. Lett.* **93**, 196104 (2004).
- [38] B.-K. Lai, I. Ponomareva, I. I. Naumov, I. Kornev, H. Fu, L. Bellaiche, and G. J. Salamo, Electric-field-induced domain evolution in ferroelectric ultrathin films, *Phys. Rev. Lett.* **96**, 137602 (2006).
- [39] Y. Nahas, S. Prokhorenko, L. Louis, Z. Gui, I. Kornev, and L. Bellaiche, Discovery of stable skyrmionic state in ferroelectric nanocomposites, *Nat. Commun.* **6**, 8542 (2015).
- [40] A. Gruverman, D. Wu, H. Fan, I. Vrejoiu, M. Alexe, R. Harrison, and J. Scott, Vortex ferroelectric domains, *J. Phys.: Condens. Matter* **20**, 342201 (2008).
- [41] B. Rodriguez, X. Gao, L. Liu, W. Lee, I. Naumov, A. Bratkovsky, D. Hesse, and M. Alexe, Vortex polarization states in nanoscale ferroelectric arrays, *Nano Lett.* **9**, 1127 (2009).
- [42] Y. Ivry, D. P. Chu, J. F. Scott, and C. Durkan, Flux closure vortexlike domain structures in ferroelectric thin films, *Phys. Rev. Lett.* **104**, 207602 (2010).
- [43] Q. Zhang, L. Xie, G. Liu, S. Prokhorenko, Y. Nahas, X. Pan, L. Bellaiche, A. Gruverman, and N. Valanoor, Nanoscale bubble domains and topological transitions in ultrathin ferroelectric films, *Adv. Mater.* **29**, 1702375 (2017).
- [44] Y. Nahas, S. Prokhorenko, J. Fischer, B. Xu, C. Carrétéro, S. Prosandeev, M. Bibes, S. Fusil, B. Dkhil, V. Garcia *et al.*, Inverse transition of labyrinthine domain patterns in ferroelectric thin films, *Nature (London)* **577**, 47 (2020).
- [45] H. Morioka, G. Asano, T. Oikawa, H. Funakubo, and K. Saito, Large remanent polarization of 100% polar-axis-oriented epitaxial tetragonal Pb(Zr_{0.35}Ti_{0.65})O₃ thin films, *Appl. Phys. Lett.* **82**, 4761 (2003).
- [46] I. Vrejoiu, G. Le Rhun, L. Pintilie, D. Hesse, M. Alexe, and U. Gösele, Intrinsic ferroelectric properties of strained tetragonal PbZr_{0.2}Ti_{0.8}O₃ obtained on layer-by-layer grown, defect-free single-crystalline films, *Adv. Mater.* **18**, 1657 (2006).
- [47] H. N. Lee, S. M. Nakhmanson, M. F. Chisholm, H. M. Christen, K. M. Rabe, and D. Vanderbilt, Suppressed dependence of polarization on epitaxial strain in highly polar ferroelectrics, *Phys. Rev. Lett.* **98**, 217602 (2007).
- [48] B. Xu, J. Íñiguez, and L. Bellaiche, Designing lead-free antiferroelectrics for energy storage, *Nat. Commun.* **8**, 15682 (2017).
- [49] Z. Jiang, Y. Nahas, S. Prokhorenko, S. Prosandeev, D. Wang, J. Íñiguez, and L. Bellaiche, Giant electrocaloric response in the prototypical Pb(Mg, Nb)O₃ relaxor ferroelectric from atomistic simulations, *Phys. Rev. B* **97**, 104110 (2018).
- [50] See Supplemental Material at <http://link.aps.org/supplemental/10.1103/PhysRevB.109.L121110> for computational details and methods, which includes Refs. [56–91].
- [51] G. Catalan, J. Seidel, R. Ramesh, and J. F. Scott, Domain wall nanoelectronics, *Rev. Mod. Phys.* **84**, 119 (2012).
- [52] F. De Guerville, I. Luk'yanchuk, L. Lahoche, and M. El Marssi, Modeling of ferroelectric domains in thin films and superlattices, *Mater. Sci. Eng.: B* **120**, 16 (2005).
- [53] I. A. Luk'yanchuk, L. Lahoche, and A. Sené, Universal properties of ferroelectric domains, *Phys. Rev. Lett.* **102**, 147601 (2009).
- [54] I. Ponomareva, I. Naumov, I. Kornev, H. Fu, and L. Bellaiche, Atomistic treatment of depolarizing energy and field in ferroelectric nanostructures, *Phys. Rev. B* **72**, 140102(R) (2005).
- [55] I. Ponomareva, I. I. Naumov, and L. Bellaiche, Low-dimensional ferroelectrics under different electrical and mechanical boundary conditions: Atomistic simulations, *Phys. Rev. B* **72**, 214118 (2005).
- [56] S. Prosandeev, S. Prokhorenko, Y. Nahas, J. Grollier, D. Talbayev, B. Dkhil, and L. Bellaiche, Ultrafast activation and tuning of topological textures in ferroelectric nanostructures, *Adv. Electron. Mater.* **8**, 2200808 (2022).
- [57] L. Nordheim, Zur elektronentheorie der metalle. I, *Ann. Phys.* **401**, 607 (1931).
- [58] A. García and D. Vanderbilt, Electromechanical behavior of BaTiO₃ from first principles, *Appl. Phys. Lett.* **72**, 2981 (1998).
- [59] B.-K. Lai, I. Ponomareva, I. Kornev, L. Bellaiche, and G. Salamo, Thickness dependency of 180° stripe domains in ferroelectric ultrathin films: A first-principles-based study, *Appl. Phys. Lett.* **91**, 152909 (2007).
- [60] L. Bellaiche, A. García, and D. Vanderbilt, Low-temperature properties of Pb(Zr_{1-x}Ti_x)O₃ solid solutions near the morphotropic phase boundary, *Ferroelectrics* **266**, 41 (2002).

- [61] M. H. Kwak, S. B. Kang, K.-C. Kim, S. Y. Jeong, S. Kim, B. H. Yoo, D. C. Chung, H. C. Ryu, D. S. Jun, M. C. Paek *et al.*, Dielectric characteristics of Pb(Zr, Ti)O₃ films on MgO single crystal substrate by terahertz time domain spectroscopy, *Ferroelectrics* **422**, 19 (2011).
- [62] S. W. Ko, W. Zhu, C. Fragkiadakis, T. Borman, K. Wang, P. Mardilovich, and S. Trolrier-McKinstry, Improvement of reliability and dielectric breakdown strength of Nb-doped lead zirconate titanate films via microstructure control of seed, *J. Am. Ceram. Soc.* **102**, 1211 (2019).
- [63] K. Y. Yun, D. Ricinchi, T. Kanashima, M. Noda, and M. Okuyama, Giant ferroelectric polarization beyond 150 $\mu\text{C}/\text{cm}^2$ in BiFeO₃ thin film, *Jpn. J. Appl. Phys.* **43**, L647 (2004).
- [64] N. J. Ramer and A. M. Rappe, Application of a new virtual crystal approach for the study of disordered perovskites, *J. Phys. Chem. Solids* **61**, 315 (2000).
- [65] R. W. Heeres and V. Zwiller, Subwavelength focusing of light with orbital angular momentum, *Nano Lett.* **14**, 4598 (2014).
- [66] A. Toma, S. Tuccio, M. Prato, F. De Donato, A. Perucchi, P. Di Pietro, S. Marras, C. Liberale, R. Proietti Zaccaria, F. De Angelis *et al.*, Squeezing terahertz light into nanovolumes: Nanoantenna enhanced terahertz spectroscopy (nets) of semiconductor quantum dots, *Nano Lett.* **15**, 386 (2015).
- [67] D. Edwards, N. Browne, K. M. Holsgrove, A. B. Naden, S. O. Sayedghaee, B. Xu, S. Prosandeev, D. Wang, D. Mazumdar, M. Duchamp *et al.*, Giant resistive switching in mixed phase BiFeO₃ via phase population control, *Nanoscale* **10**, 17629 (2018).
- [68] Y. Nahas, S. Prokhorenko, Q. Zhang, V. Govinden, N. Valanoor, and L. Bellaiche, Topology and control of self-assembled domain patterns in low-dimensional ferroelectrics, *Nat. Commun.* **11**, 5779 (2020).
- [69] P. Chen, C. Paillard, H. J. Zhao, J. Íñiguez, and L. Bellaiche, Deterministic control of ferroelectric polarization by ultrafast laser pulses, *Nat. Commun.* **13**, 2566 (2022).
- [70] V. Garcia and M. Bibes, Ferroelectric tunnel junctions for information storage and processing, *Nat. Commun.* **5**, 4289 (2014).
- [71] A. Chanthbouala, A. Crassous, V. Garcia, K. Bouzouane, S. Fusil, X. Moya, J. Allibe, B. Dlubak, J. Grollier, S. Xavier *et al.*, Solid-state memories based on ferroelectric tunnel junctions, *Nat. Nanotechnol.* **7**, 101 (2012).
- [72] D. K. Gramotnev and S. I. Bozhevolnyi, Plasmonics beyond the diffraction limit, *Nat. Photon.* **4**, 83 (2010).
- [73] L. Novotny and N. Van Hulst, Antennas for light, *Nat. Photon.* **5**, 83 (2011).
- [74] V. Garcia, S. Fusil, K. Bouzouane, S. Enouz-Vedrenne, N. D. Mathur, A. Barthelémy, and M. Bibes, Giant tunnel electroresistance for non-destructive readout of ferroelectric states, *Nature (London)* **460**, 81 (2009).
- [75] A. Rusina, M. Durach, K. A. Nelson, and M. I. Stockman, Nanoconcentration of terahertz radiation in plasmonic waveguides, *Opt. Express* **16**, 18576 (2008).
- [76] F. Mayer, M. Deluca, and M. N. Popov, Hidden phases in homovalent and heterovalent substituted BaTiO₃, *Phys. Rev. B* **107**, 184307 (2023).
- [77] L. Bellaiche and D. Vanderbilt, Virtual crystal approximation revisited: Application to dielectric and piezoelectric properties of perovskites, *Phys. Rev. B* **61**, 7877 (2000).
- [78] L. Bellaiche, A. García, and D. Vanderbilt, Electric-field induced polarization paths in Pb(Zr_{1-x}Ti_x)O₃ alloys, *Phys. Rev. B* **64**, 060103(R) (2001).
- [79] A. Schilling, T. B. Adams, R. M. Bowman, J. M. Gregg, G. Catalan, and J. F. Scott, Scaling of domain periodicity with thickness measured in BaTiO₃ single crystal lamellae and comparison with other ferroics, *Phys. Rev. B* **74**, 024115 (2006).
- [80] I. Ponomareva and L. Bellaiche, Nature of dynamical coupling between polarization and strain in nanoscale ferroelectrics from first principles, *Phys. Rev. Lett.* **101**, 197602 (2008).
- [81] H. Béa, B. Dupé, S. Fusil, R. Mattana, E. Jacquet, B. Warot-Fonrose, F. Wilhelm, A. Rogalev, S. Petit, V. Cros *et al.*, Evidence for room-temperature multiferroicity in a compound with a giant axial ratio, *Phys. Rev. Lett.* **102**, 217603 (2009).
- [82] D. Sichuga and L. Bellaiche, Epitaxial Pb(Zr, Ti)O₃ ultrathin films under open-circuit electrical boundary conditions, *Phys. Rev. Lett.* **106**, 196102 (2011).
- [83] R. Mankowsky, A. von Hoegen, M. Först, and A. Cavalleri, Ultrafast reversal of the ferroelectric polarization, *Phys. Rev. Lett.* **118**, 197601 (2017).
- [84] L. Lu, Y. Nahas, M. Liu, H. Du, Z. Jiang, S. Ren, D. Wang, L. Jin, S. Prokhorenko, C.-L. Jia *et al.*, Topological defects with distinct dipole configurations in PbTiO₃/SrTiO₃ multilayer films, *Phys. Rev. Lett.* **120**, 177601 (2018).
- [85] S. Prosandeev, J. Grollier, D. Talbayev, B. Dkhil, and L. Bellaiche, Ultrafast neuromorphic dynamics using hidden phases in the prototype of relaxor ferroelectrics, *Phys. Rev. Lett.* **126**, 027602 (2021).
- [86] L. Bellaiche, A. García, and D. Vanderbilt, Finite-temperature properties of Pb(Zr_{1-x}Ti_x)O₃ alloys from first principles, *Phys. Rev. Lett.* **84**, 5427 (2000).
- [87] S. K. Streiffer, J. A. Eastman, D. D. Fong, C. Thompson, A. Munkholm, M. V. Ramana Murty, O. Auciello, G. R. Bai, and G. B. Stephenson, Observation of nanoscale 180° stripe domains in ferroelectric PbTiO₃ thin films, *Phys. Rev. Lett.* **89**, 067601 (2002).
- [88] C. Ederer and N. A. Spaldin, Effect of epitaxial strain on the spontaneous polarization of thin film ferroelectrics, *Phys. Rev. Lett.* **95**, 257601 (2005).
- [89] G. Spektor, D. Kilbane, A. Mahro, B. Frank, S. Ristok, L. Gal, P. Kahl, D. Podbiel, S. Mathias, H. Giessen *et al.*, Revealing the subfemtosecond dynamics of orbital angular momentum in nanoplasmonic vortices, *Science* **355**, 1187 (2017).
- [90] M. Pu, X. Ma, Z. Zhao, X. Li, Y. Wang, H. Gao, C. Hu, P. Gao, C. Wang, and X. Luo, Near-field collimation of light carrying orbital angular momentum with bull's-eye-assisted plasmonic coaxial waveguides, *Sci. Rep.* **5**, 12108 (2015).
- [91] D. Garoli, P. Zilio, Y. Gorodetski, F. Tantussi, and F. De Angelis, Optical vortex beam generator at nanoscale level, *Sci. Rep.* **6**, 29547 (2016).